

<https://doi.org/10.1038/s43247-025-03009-2>

Natural ocean alkalization through erosion of glacial till and weathering at the seafloor

Check for updates

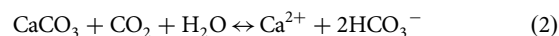
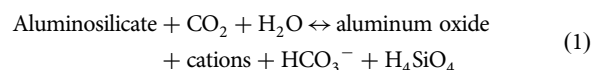
Florian Scholz ¹ ✉, Janine Börker¹, Christoph Vogt ^{2,3}, Jens Hartmann¹ & Klaus Wallmann ⁴

The ocean absorbs about 25% of anthropogenic carbon dioxide emissions, with this uptake regulated by acid-neutralizing anions collectively termed alkalinity. Most seawater alkalinity originates from the weathering of aluminosilicate and carbonate minerals on land, whose dissolved products are transported to the ocean by rivers, a slow process that causes carbon dioxide removal to lag behind emissions. Here we present geochemical evidence showing that fine-grained glacial sediments mobilized by coastal erosion undergo rapid seafloor weathering. While aluminosilicate weathering is largely balanced by secondary clay formation (reverse weathering), carbonate dissolution yields a significant net release of alkalinity to coastal waters. Because more than two-thirds of the global coastline was formerly glaciated, ongoing deglaciation and erosion may enhance alkalinity fluxes, providing a previously unrecognized shortcut in the global carbon cycle. As this enhanced flux is ultimately driven by climate warming, it may act as a negative feedback that helps moderate future increases in atmospheric carbon dioxide.

High-latitude coastal areas are currently experiencing rapid environmental change. The combined effects of retreating sea ice, permafrost thaw, deglaciation, sea-level rise, isostatic rebound, and increased precipitation are expected to accelerate the transfer of terrigenous material to coastal oceans, mobilized from river catchments and eroding shorelines^{1–4}. Previous studies have primarily explored how these trends influence the transfer of nutrients^{5,6} and carbon^{7–9} to coastal waters, as well as their impact on the biological carbon pump. Findings are ambiguous, suggesting an increase in primary productivity but a limited or even reversed effect on carbon export due to a warming-induced rise in respiration^{10–12}.

An aspect that has received considerably less attention is the impact of climate change-induced erosion on inorganic carbon cycling in continental shelf sediments. The land surface exposed by retreating glaciers is covered with glacial till, a fine-grained lithogenic material that was transported and ground beneath the glacier. Due to their high surface area, minerals in fine-grained glacial deposits are generally more reactive compared to those in other Earth surface environments^{13,14}. Many aluminosilicate minerals contained in glacial till may be undersaturated in seawater and therefore prone to dissolution (i.e., weathering)^{15,16}. In addition, the buildup of metabolic CO₂ from aerobic organic matter degradation in bottom waters and sediment pore waters may lead to undersaturation and subsequent dissolution of carbonate minerals present in the till. Weathering of aluminosilicate and

carbonate minerals converts CO₂ to HCO₃[−] (i.e., alkalinity) and releases silicic acid (H₄SiO₄) and dissolved cations (e.g., Na⁺, K⁺, Mg²⁺, Ca²⁺) to solution:



By consuming CO₂ and generating HCO₃[−], weathering of glacial debris at the seafloor could mitigate ocean acidification and enhance the buffering and CO₂ uptake capacity of coastal seawater. Overall, this natural scenario resembles artificial methods of carbon dioxide removal, in which alkaline minerals are distributed at the seafloor to induce weathering and alkalinity production^{17,18}. However, unlike artificial ocean alkalinity enhancement (OAE), the delivery of weatherable glacial debris in this case is intrinsically linked to warming-induced erosion. As a result, weathering of glacial debris could function as a negative feedback mechanism in the Earth system, where rising atmospheric CO₂ enhances erosion, accelerates seafloor weathering, and ultimately increases CO₂ removal.

Some of the effect of seafloor weathering on oceanic alkalinity may be counteracted by the neoformation of secondary (authigenic) minerals^{19–23}.

¹Department of Earth System Sciences, Center for Earth System Research and Sustainability (CEN), University of Hamburg, Hamburg, Germany. ²Crystallography and Geomaterials Research, FB05 Geosciences, University of Bremen, Bremen, Germany. ³MARUM Center for Marine Environmental Sciences, Leobener Straße, Bremen, Germany. ⁴GEOMAR Helmholtz Centre for Ocean Research Kiel, Wischhofstraße 1-3, Kiel, Germany. ✉e-mail: florian.scholz@uni-hamburg.de

High cation concentrations in seawater, combined with HCO_3^- production from anaerobic organic matter degradation^{24,25} and release of dissolved silica from dissolution of biogenic opal^{16,27}, can cause pore waters to become oversaturated with respect to authigenic clay or carbonate minerals, shifting the equilibrium described in Eqs. 1 and 2 to the left. Since precipitation of authigenic aluminosilicate minerals consumes alkalinity and releases CO_2 , this process is referred to as reverse weathering^{20,21}. Depending on the balance between weathering and reverse weathering, alteration of glacial debris could act as either a net source or net sink for CO_2 .

Quantifying weathering-derived HCO_3^- fluxes in marine sediments is challenging due to the additional alkalinity produced by anaerobic degradation of organic matter. As an alternative approach, and building on weathering studies in river catchments^{28,29}, cation fluxes and charge balance constraints, where net cation charge must be matched by HCO_3^- , can be employed to quantify the overall effect of mineral alteration on inorganic carbon turnover^{16,30}. The cations released from primary minerals often differ from those sequestered by secondary minerals. Consequently, mineral alteration occurring at the seafloor can lead to substantial cation fluxes, regardless of whether the net process is classified as weathering or reverse weathering.

In this study, we investigate how erosion of glacial till at sea cliffs and mineral alteration processes at the seafloor influence cation and alkalinity fluxes in the coastal ocean. We explore the interplay between weathering and reverse weathering, considering sediment transport dynamics and

biogenic sedimentation. Our findings reveal that in dynamic shelf systems with moderate organic matter turnover, aluminosilicate and carbonate minerals in glacial sediments can rapidly dissolve at the seafloor, potentially generating substantial fluxes of cations and alkalinity.

Environmental setting

Vast areas of northern Europe are covered by glacial deposits, which were delivered by the Scandinavian Ice Sheet during the late Pleistocene (Fig. 1A). Along the southwestern Baltic Sea coast, glacial deposits have a broad grain-size spectrum and form coastal cliffs reaching heights of up to 25 m (Fig. 1B, C). During storm surges, waves and currents erode the foot of the cliffs (Fig. 1C–E), resulting in a mean coastal retreat rate of 0.24 m yr^{-1} ^{31,32}. Due to the low permeability of the glacial till and continuous erosion exposing fresh surfaces, the eroded material retains a relatively pristine composition closely resembling the felsic igneous and metamorphic source rocks in Scandinavia³³. In addition to felsic material from Scandinavia, the glaciers eroded limestone from the Baltic Sea basin, adding ground carbonate minerals to the till. As a result, the predominant minerals in the glacial till are quartz (~57%), feldspars (~16%), calcite (~12%) and muscovite (~10%) (Table S1)³⁴. Upon erosion, the coarse-grained material (rock fragments and sand) is retained in shallow and near-shore areas, while the finer silt- and clay-sized particles are transported further offshore to accumulate along with marine biogenic material (organic matter and biogenic opal) in depocenters below ~25 m water depth (Fig. 1B)³⁴. With no major rivers

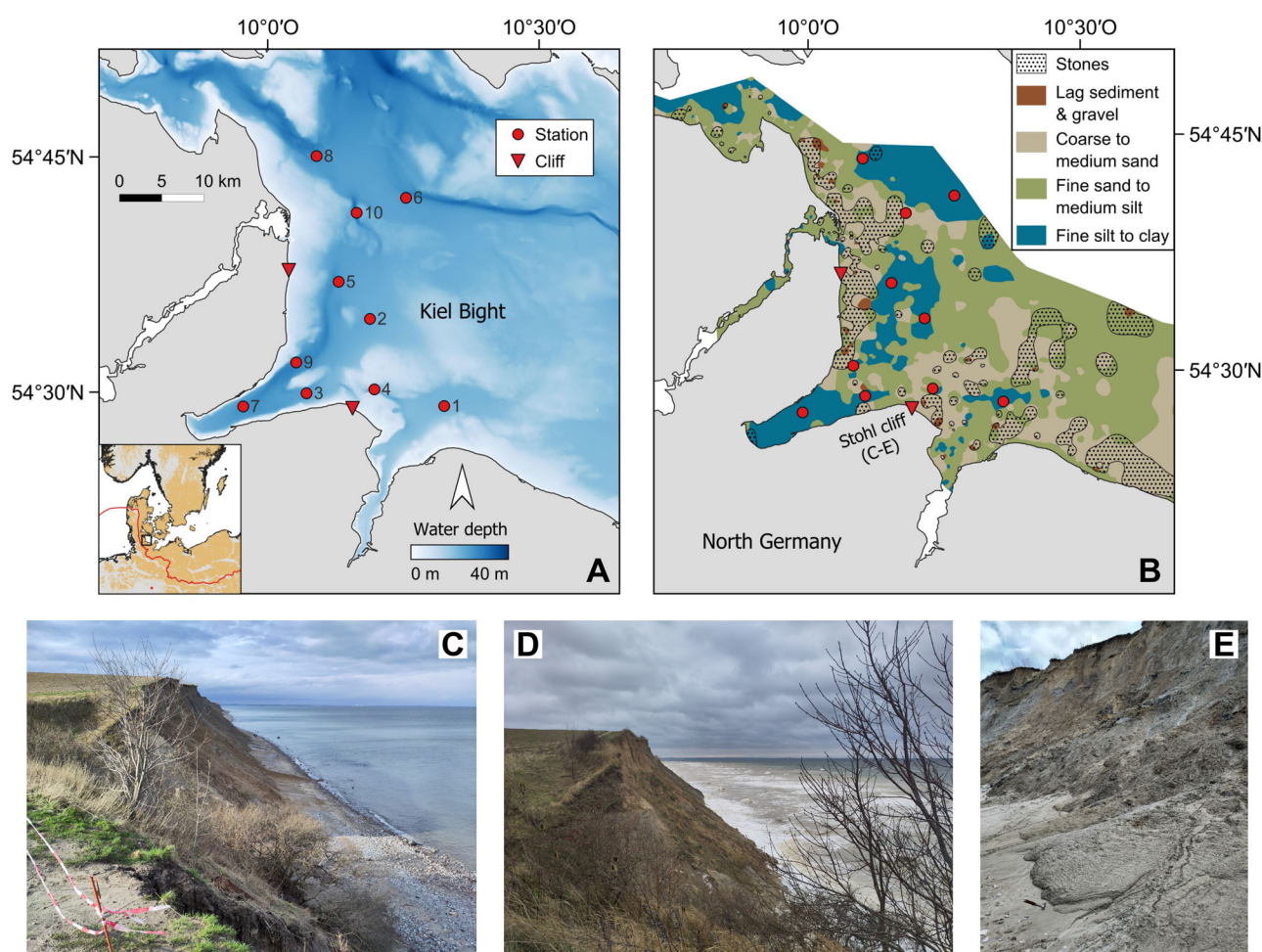


Fig. 1 | Study area in the southwestern Baltic Sea. A Bathymetric map of Kiel Bight. Major coastal cliffs and coring locations are marked by triangles and circles, respectively. The red line on the inset map shows the maximum extent of the Scandinavian Ice Sheet during the Last Glacial Maximum (LGM)³³. Colored land areas represent unconsolidated glacial deposits⁵⁵. **B** Distribution of sediment types in

Kiel Bight⁴⁶. **C** Photographs of the coastal cliff in Stohl under calm weather conditions, with a visible talus of eroded material at its base. **D** The same coastal cliff during a storm surge, showing a submerged beach and active erosion. **E** Liquefied till flowing from the cliff's talus into the swash zone.

discharging into the southwestern Baltic Sea, coastal erosion is the predominant sediment source to our study area, the Kiel Bight. Elevated nutrient concentrations drive intense biological productivity, leading to substantial organic matter delivery to deeper waters and sediments^{35,36}. Due to the combined effects of high oxygen demand and restricted water exchange through the Danish Straits, deeper water layers experience seasonal oxygen depletion³⁷. To investigate geochemical interactions between glacial till and seawater, samples were collected at two major cliffs and 10 sediment cores were retrieved and sequentially numbered by increasing water depth (Fig. 1).

Results and discussion

Evidence for rapid mineral alteration at the seafloor

Sediments in Kiel Bight are enriched in Mg but depleted in K and Ca relative to the glacial till (Fig. 2). Sedimentary Mg concentrations increase, while those of K decrease gradually with water depth. Ca remains uniformly depleted, except at station 7, where concentrations are slightly higher compared to the other sites. Those major element trends could, in principle, result from mineral alteration or current-induced lateral grain-size sorting. However, because Mg, K and Ca are predominantly contained in the fine-grained sediment fraction³⁶ it is unlikely that K and Ca are retained in sandy near-shore areas while Mg is concentrated at greater depth (see Fig. S1 and Table S1 for further details on grain-size sorting).

In-situ dissolution or precipitation of minerals should be reflected in cation release to or removal from pore water. Consistent with solid-phase observations, pore water Mg^{2+} concentrations decrease with sediment depth, whereas K^+ concentrations show the opposite trend (Fig. 3). Such major cation anomalies are occasionally found in pore waters of deeper (ranging from meters to tens of meters) methanic sediments, where they indicate the in-situ dissolution or precipitation of aluminosilicate minerals^{38–40}. Detecting anomalies in major cation concentrations in shallow pore waters of rapidly accumulating near-shore sediments indicates that mineral alteration proceeds at a high rate soon after deposition. Shallow anomalies of pore water K^+ concentrations have been observed on (sub) tropical river shelves^{41–43}. However, unlike the present study, pore waters in these systems are depleted in K^+ , indicating that different processes are at play.

Pore water concentrations of Mg^{2+} and K^+ evolve asymptotically with depth, eventually reaching a stable value (Fig. 3). This downcore distribution closely mirrors that of H_4SiO_4 , which is primarily released into the pore water through the dissolution of biogenic opal. However, H_4SiO_4 concentrations remain below the theoretical solubility of biogenic opal at ambient pressure and temperature. This observation suggests that the concentrations of these three solutes are governed by the saturation state of silicate minerals. To identify terrigenous minerals that may dissolve to release K^+ and authigenic minerals that precipitate to sequester Mg^{2+} , we included our pore water data into the geochemical model PHREEQC⁴⁴. The

clay mineral illite, a disordered variant of the K-rich mica muscovite, is strongly undersaturated in surface sediments (0–3 cm) but approaches equilibrium at greater depth (Fig. 3). By contrast, hydrous Mg-rich montmorillonite, a prevalent clay mineral of the smectite group, is markedly oversaturated throughout the sediment column, especially in the deeper layers (>3 cm) (Fig. 3). These contrasting saturation states suggest that the observed anomalies in Mg^{2+} and K^+ concentrations in both pore water and solid can be attributed to a combination of illite dissolution and montmorillonite precipitation.

Pore water Ca^{2+} profiles increase with depth, especially at the shallower stations (Fig. 3). Unlike the glacial till, fine-grained sediments in Kiel Bight contain very little calcite, and Ca concentrations strongly correlate with inorganic carbon (Fig. S2). These observations align with previous studies suggesting that calcium carbonate eroded from coastal cliffs undergoes dissolution on the seafloor of the Baltic Sea⁴⁵. Contrary to earlier hypotheses, however, the majority of carbonate dissolution does not occur in sediment depocenters with high biogenic sedimentation (>25 m water depth). Instead, the almost uniform Ca depletion in sediments across Kiel Bight (Fig. 2) suggests that the dissolution of cliff-derived carbonate already happens during its passage through shallower areas. Below 10 m water depth, oxygen depletion (Fig. S2) and the resulting accumulation of metabolic CO_2 lead to general undersaturation with respect to calcite in both bottom waters and surface sediments across all stations (Fig. 3). Rapid carbonate dissolution in the shallower areas may be facilitated by aerobic respiration in more permeable sediments⁴⁶ and may also be enhanced by frequent re-suspension and transport driven by bottom currents. In contrast, in the organic matter-rich depocenters at greater depths, intense microbial sulfate reduction in subsurface sediments generates alkalinity (Fig. 3), thereby shifting the carbonate equilibrium (Eq. 2) toward preservation or even authigenic precipitation rather than dissolution^{24,47}. Authigenic carbonate precipitation is particularly evident at station 7, where near-complete sulfate depletion coincides with peak alkalinity, pronounced calcite oversaturation (Fig. 3), and elevated solid-phase Ca concentrations (Fig. 2).

Weathering versus reverse weathering

We find evidence for both the dissolution of aluminosilicate and carbonate minerals delivered by cliff erosion and the precipitation of authigenic minerals. To evaluate the net alkalinity flux associated with aluminosilicate alteration, we quantified the rates of K^+ release and Mg^{2+} fixation using a reaction-transport model (RTM) fitted to pore water profiles averaged across the study area (Fig. 3). Due to limited bioturbation in oxygen-deficient bottom waters, depth-integrated rates of cation release and fixation correspond to cation fluxes across the sediment-water interface. Because the pore water K^+ gradient was steeper than that of Mg^{2+} (Fig. 3), the mean K^+ release rate ($-856 \text{ mmol m}^{-2} \text{ yr}^{-1}$) exceeds the Mg^{2+} fixation rate ($254 \text{ mmol m}^{-2} \text{ yr}^{-1}$). When adjusted for cation charge, this results in a net alkalinity flux of $-348 \text{ meq m}^{-2} \text{ yr}^{-1}$. The negative sign implies that, at

Fig. 2 | Geochemistry of marine sediments compared to the glacial till. Box plot of element concentrations normalized to aluminum (Al) for all sediment cores, arranged in order of increasing water depth. The vertical dashed line illustrates the composition of the glacial till. In contrast to Mg, K and Ca, Al has a low solubility in seawater at circumneutral pH. Therefore, normalizing major element concentrations to Al helps differentiate mineral alteration signals from variable dilution by biogenic material.

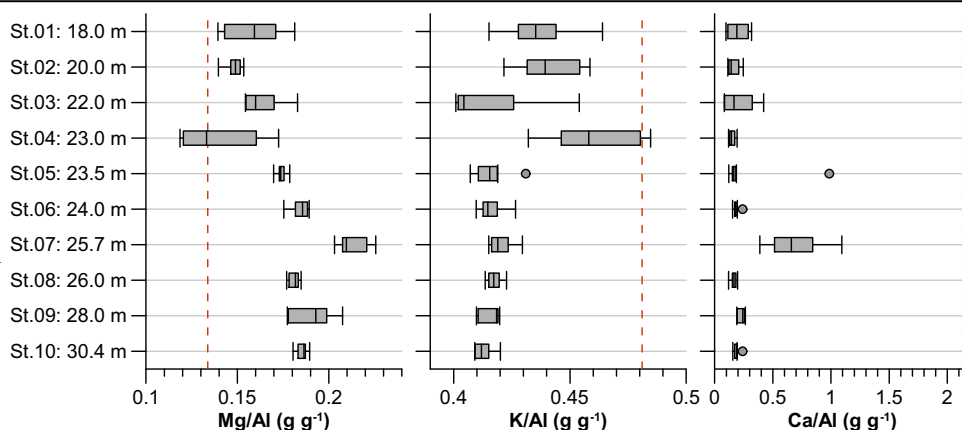
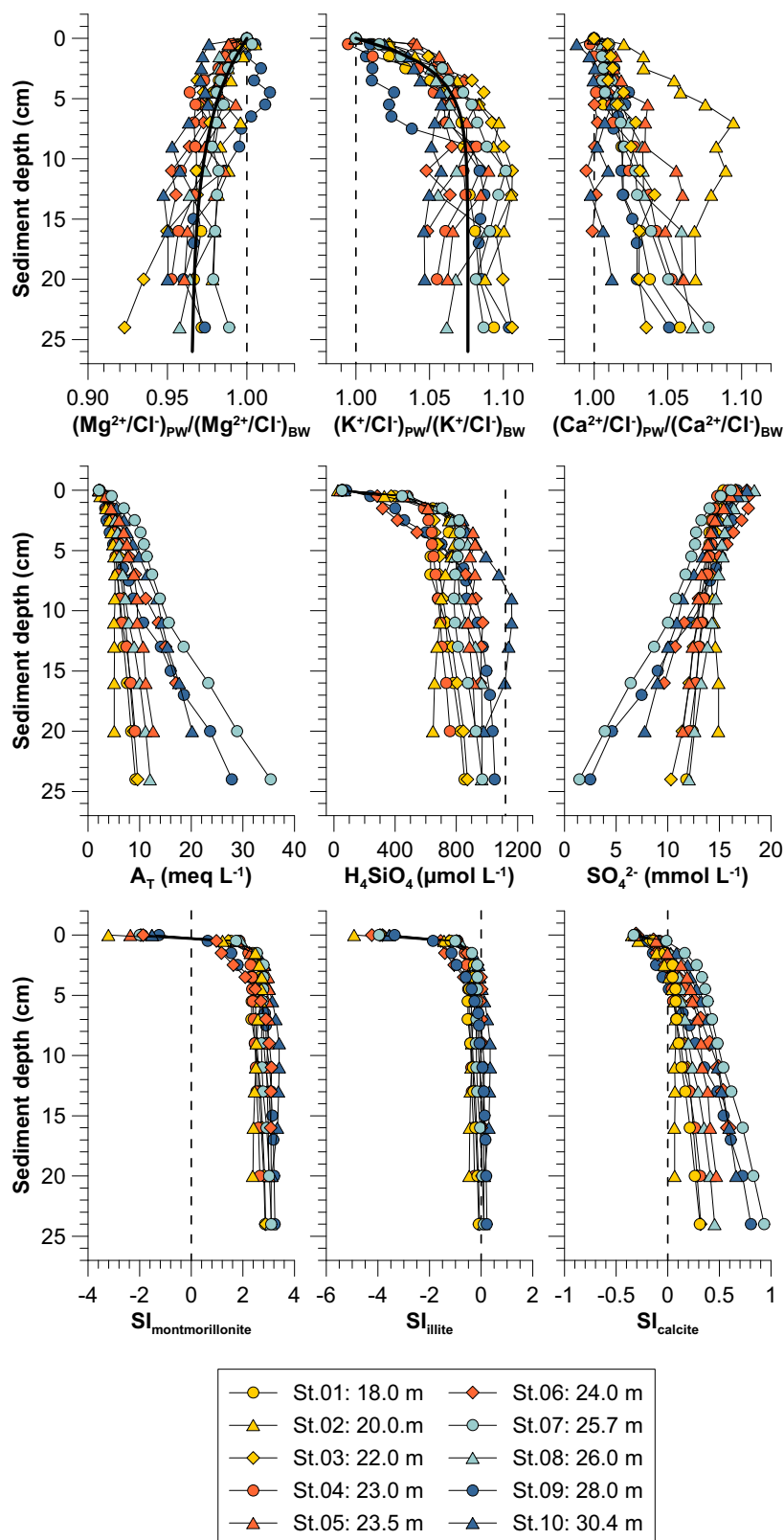


Fig. 3 | Pore water geochemistry. Upper row: Pore water profiles of the major cations (Mg^{2+} , K^+ and Ca^{2+}) normalized to chloride (Cl^-). Since Cl^- is influenced only by salinity and does not participate in mineral alteration processes, normalizing major cations to Cl^- helps distinguish mineral alteration signals from salinity fluctuations caused by seawater inflow via the Danish Straits. To highlight downcore trends, cation-to- Cl^- ratios in pore water (PW) samples are divided by the corresponding ratios in bottom water (BW). Dashed lines indicate bottom water composition. Solid black lines in the Mg^{2+}/Cl^- and K^+/Cl^- profiles were used to derive rates of Mg^{2+} fixation and K^+ release using a reaction-transport model. Middle row: pore water profiles of total alkalinity (A_T), H_4SiO_4 and SO_4^{2-} . The vertical dashed line in the H_4SiO_4 diagram indicates the theoretical solubility of biogenic opal at ambient pressure and temperature, assuming a specific surface area of $25\text{ m}^2\text{ g}^{-1}$ ⁶⁷. Lower row: pore water saturation state of hydrous montmorillonite, illite and calcite. A saturation index (SI) below zero indicates undersaturation and potential mineral dissolution whereas an SI above zero indicates oversaturation and potential mineral precipitation. Dashed lines indicate equilibrium (SI = 0).



the time of sampling, the dominant mineral alteration process was weathering, which consumes CO_2 and generates alkalinity. Additional alkalinity may be supplied by weathering of Na-containing plagioclase feldspar (albite), which was also undersaturated in surface sediments of Kiel Bight (Fig. S4). However, the downcore profiles of Na in both the pore water and solid phase are inconclusive, and therefore, this process is not included in the

charge budget. For context, the alkalinity flux related to aluminosilicate weathering corresponds to $\sim 10\%$ of the alkalinity flux generated by anaerobic organic matter degradation in sediments of Kiel Bight, as estimated at Station 9 using an RTM⁴⁷.

To evaluate the long-term spatial balance between cation release and fixation, we analyze the distribution of K and Mg anomalies in the solid

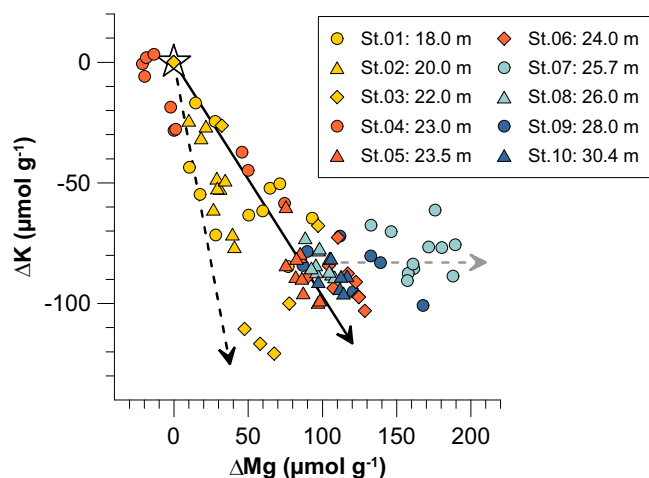


Fig. 4 | Stoichiometric trends resulting from mineral alteration. Deviation of sedimentary K and Mg concentrations from the composition of glacial till plotted against each other. Stoichiometric trends of aluminosilicate alteration (K^+ release and Mg^{2+} uptake) are derived from the reaction-transport model (black dashed line) and mineral equilibria defined in the database of the geochemical model PHREEQC (Eqs. 5 and 6), assuming that all Al released from illite is incorporated into hydrous montmorillonite (black solid line). Authigenic carbonate minerals precipitating at high alkalinities incorporate Mg but not K, resulting in a horizontal trend (gray dashed line).

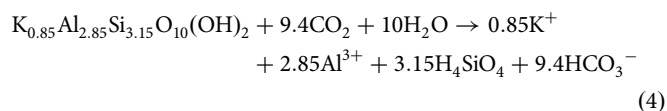
phase using a cross-plot (Fig. 4). The deviation in sedimentary element concentration from glacial till (ΔE) was calculated using the following equation, assuming that the aluminum (Al) concentration is conserved during mineral alteration and mixing with biogenic material:

$$\Delta E = E_{\text{sediment}} - \left(\frac{E}{Al} \right)_{\text{glacial till}} \cdot Al_{\text{sediment}} \quad (3)$$

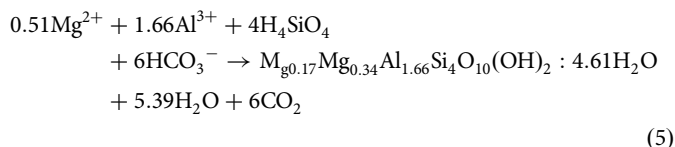
The stoichiometric trend derived from fitting the RTM to our pore water data ($\Delta K:\Delta Mg = -856:254 = -3.37$) represents the upper range of ratios observed in the solid phase (Fig. 4). This trend aligns primarily with samples from shallower water depth (stations 1–4) (Fig. 1). In contrast, at greater water depths, where the majority of the fine-grained sediment accumulates, most samples exhibit a lower $\Delta K:\Delta Mg$. We thus observe a spatial decoupling of cation release and fixation across Kiel Bight.

Surface sediments in Kiel Bight (0–3 cm) host a transition from strong illite undersaturation to pronounced montmorillonite oversaturation (Fig. 3). At shallower stations, illite dissolution and the associated release of K^+ at the sediment surface may be intensified by stronger bottom currents, which increase grain collisions and repeatedly disrupt the diffusive boundary layer surrounding sediment particles during sediment resuspension and transport⁴⁸. These processes produce a cation-depleted, Al-rich residue that is either buried deeper in the sediment column or transported downslope. At greater sediment depths, and in depocenters characterized by high biogenic sedimentation, H_4SiO_4 accumulation from opal dissolution leads to montmorillonite oversaturation, thereby promoting Mg uptake. In these settings, where H_4SiO_4 is abundant, the extent of montmorillonite formation is likely limited by the availability of reactive Al derived from illite dissolution (Eq. 1).

According to the equilibrium defined in PHREEQC, illite dissolution liberates K^+ and Al^{3+} in a ratio of $\Delta K:\Delta Al = 0.85:2.85 = 0.30$:



The precipitation of hydrous montmorillonite removes Mg^{2+} and Al^{3+} in a ratio of $\Delta Mg:\Delta Al = 0.51:1.66 = 0.31$:



Dividing $\Delta K:\Delta Al$ ratio from illite dissolution by the $\Delta Mg:\Delta Al$ from montmorillonite precipitation results in a $\Delta K:\Delta Mg$ ratio of $(-0.97$ for the coupled reaction. This ratio aligns with most sediment samples from deeper areas (stations 5–10) with high biogenic sedimentation (Fig. 4). Our analysis confirms that, when the rate of H_4SiO_4 supply by biogenic opal dissolution is high, Al^{3+} from illite dissolution becomes the limiting factor for montmorillonite precipitation. Due to the higher charge of Mg^{2+} compared to K^+ , an approximately equal amount of K^+ released and Mg^{2+} consumed results in a net sink of positive charge and, consequently, a net reduction of alkalinity by reverse weathering.

Under Al limitation, the alkalinity consumption by reverse weathering likely depends on the difference in the cation charge-to-Al ratio between the dissolving and precipitating minerals. Given that illite has a lower cation charge-to-Al ratio than montmorillonite (0.30 vs. 0.62), the long-term spatial balance is positive, resulting in a net sink for alkalinity. By contrast, if the dissolving mineral does not contain Al (e.g., olivine, $(Fe,Mg)_2SiO_4$) or has a higher cation charge-to-Al ratio than montmorillonite (e.g., plagioclase feldspar, $CaAl_2Si_2O_8$; 1.0), the charge balance is negative, resulting in a net source of alkalinity.

Several samples in Fig. 4 show an increase in ΔMg without a corresponding rise in ΔK , particularly those from station 7. This pattern is not associated with aluminosilicate alteration but rather reflects the in-situ precipitation of carbonate minerals driven by intense sulfate reduction. Authigenic carbonate minerals incorporate Mg but not $K^{49,50}$, resulting in a horizontal trend in Fig. 4. However, across all sites in Kiel Bight, sediments are depleted in Ca relative to the glacial till, indicating that the near-complete dissolution of terrigenous carbonate substantially exceeds the extent of authigenic carbonate precipitation (Fig. 2).

The solid-phase composition at station 10, the deepest of our coring sites, can be used to quantify the overall cation balance resulting from till erosion, aluminosilicate alteration, carbonate dissolution and transport into the terminal depocenter (Fig. 2). Changes in the solid-phase composition relative to the glacial till (Eq. 3) are calculated as $\Delta K = -82.9 \pm 5.4 \mu\text{mol g}^{-1}$, $\Delta Mg = 99.2 \pm 6.5 \mu\text{mol g}^{-1}$ and $\Delta Ca = -2500 \pm 6.5 \mu\text{mol g}^{-1}$. Multiplying these numbers by the respective cation charges and summing up results in an overall charge flux of -4.89 meq g^{-1} . This calculation indicates that 4.89 meq of alkalinity are released per gram of fine-grained glacial till eroded. As reverse weathering ultimately outcompetes aluminosilicate weathering over the long term, this net alkalinity flux is attributed entirely to carbonate dissolution.

Significance of cation and alkalinity fluxes from glacial sediments

Pore water geochemical data capture a snapshot of current conditions, whereas the solid phase composition reflects sediment-seawater interactions over decadal timescales. The generally consistent geochemical signals observed in both pore water and solid phase indicate that mineral alteration at the seafloor in Kiel Bight is a continuous process rather than being limited to episodic events²². Furthermore, aluminosilicate alteration predominantly occurs in surface sediments rather than within the deeper methanic zone^{38–40}, highlighting the sustained high reactivity of glacial till even 19,000 years after the final retreat of the Scandinavian Ice Sheet³³. In Kiel Bight, weathering and reverse weathering processes are closely coupled, resulting in minimal inorganic carbon turnover associated with aluminosilicate alteration. In contrast, carbonate dissolution represents a net source of

alkalinity, highlighting the potential of calcium carbonate as an effective raw material for artificial OAE in the Baltic Sea^{47,51}. Our findings suggest that the scope of potential OAE target sites should be broadened to include dynamic sedimentary environments, where the interplay of aerobic respiration and frequent sediment reworking and transport enhances mineral dissolution efficiency.

Quantifying the global impact of till erosion and subsequent mineral weathering at the seafloor on cation and alkalinity fluxes is difficult for two main reasons: (i) the lack of reliable global mass flux estimates from coastal erosion⁵² and (ii) the substantial variability in seafloor weathering intensity, which is controlled by both sediment weatherability and the rate of organic matter degradation³⁹. To approximate the global seafloor area where fine-grained glacial sediments may interact with seawater, we determined the overlap between the global ice sheets during the Last Glacial Maximum (LGM)⁵³ and the present-day continental shelf⁵⁴ (Fig. 5). This overlap covers 9.44×10^6 km², or ~30% of the global shelf area. The corresponding coastline extends 1.00×10^6 km, equivalent to 72% of the global coastline. Glacial unconsolidated deposits cover large parts of the adjacent land areas⁵⁵ (Fig. 5). Along formerly glaciated coastlines, the predominant bedrock lithology is carbonate-bearing sedimentary rocks (22%), followed by metamorphic rocks (20%), siliciclastic sedimentary rocks (9.8%), felsic igneous rocks (9.2%) and mafic igneous rocks (5.0%)⁵⁶. The sheer length of the formerly glaciated coastline, together with the widespread occurrence of glacial deposits, carbonates, and other weatherable lithologies along these margins, highlights the global significance of the seafloor weathering processes observed in the southwestern Baltic Sea.

Our seafloor K flux estimates highlight the potential role of till erosion and seafloor weathering in regulating seawater cation budgets. Current estimates of the global marine K cycle indicate a substantial imbalance, where the uptake of K by authigenic clay minerals (-2.5 ± 1.0 Tmol yr⁻¹)

significantly exceeds the K⁺ supply from rivers (1.2 Tmol yr⁻¹)¹⁶. However, these estimates typically assume that terrigenous particles act as sinks for K⁺ upon contact with seawater and during early diagenesis in marine sediments. In contrast, our findings suggest that weathering of fine-grained, felsic (i.e., K-rich) material of glacial origin can represent a substantial source of K⁺ to coastal seawater. The K⁺ release rate observed in Kiel Bight (-856 mmol m⁻² yr⁻¹) is comparable in magnitude to the rate of K⁺ uptake by shallow sediments on the Amazon shelf (1100 mmol m⁻² yr⁻¹)⁴². Enhanced release of K from felsic minerals in glacial sediment is likely driven by the low extent of terrestrial chemical weathering in glaciated regions compared to river catchments at lower latitudes^{23,39}. Multiplying the proportion of felsic igneous rocks in past glaciated areas (9.2%)⁵⁶ by the ice-covered shelf area during the LGM and the mean benthic K flux observed in this study yields a global K flux of 0.74 Tmol yr⁻¹. This K flux, potentially derived from the weathering of glacial sediments, may represent a previously underappreciated source of K to the ocean and could contribute to closing the marine K budget.

Upscaling alkalinity fluxes from weathering of glacial sediments at the seafloor is complicated by the poorly constrained balance between weathering and reverse weathering at the global scale^{16,23}. Our findings indicate that coastal erosion and weathering of calcium carbonate and cation-rich aluminosilicate minerals may represent a relevant source of alkalinity to coastal waters. This contribution could be further amplified by climate change-driven increases in coastal erosion and land-to-ocean material fluxes at high latitudes. Consistent with this notion, elevated alkalinity levels have been reported in recent decades in both the Baltic Sea⁵⁷ and the Arctic North Atlantic⁵⁸. Alkalinity generated by the weathering of glacial sediments can directly enhance the buffering capacity of coastal seawater, potentially establishing a negative feedback mechanism by promoting additional CO₂ uptake from the atmosphere. Further investigation of mineral alteration

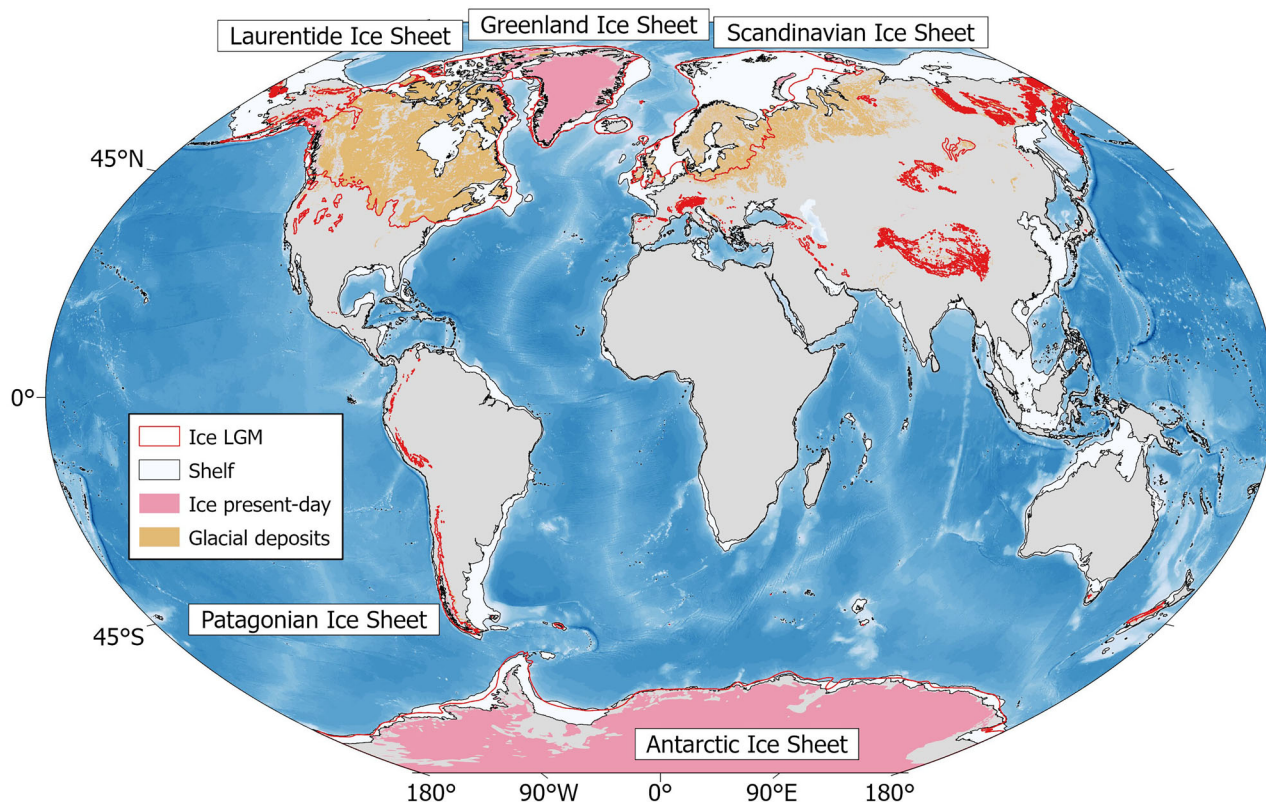


Fig. 5 | Global map showing continental shelf areas with glacial sediments. The present-day continental shelf⁵⁴ is highlighted in white with black borders. Shelf areas outlined in red indicate regions that were covered by ice sheets during the Last Glacial Maximum (LGM)⁵³. Adjacent coastal areas are largely composed of glacial

unconsolidated deposits or glaciers⁵⁵, suggesting that the terrigenous sediments in these shelf regions predominantly originate from glacial deposits. Detailed information on the dominant bedrock lithologies along formerly glaciated coastlines is provided in Supplementary Table S3.

processes in high-latitude coastal environments is therefore essential to better quantify these fluxes and to assess their role in the global carbon cycle during both present and past episodes of climate warming.

Material and methods

Sampling and chemical analyses

Glacial till samples ($n = 36$) were collected in September 2021 at two major coastal cliffs in Kiel Bight. Water column and sediment samples were retrieved in August 2020 during the RV Alkor cruise AL543 (Table S2). A CTD was deployed to measure temperature, salinity and oxygen concentrations. A multiple corer was used to retrieve sediment cores with an undisturbed sediment-water interface. The bottom water was siphoned with a plastic tube and subsequently treated like pore water samples. Sediment subsampling was realized at in situ temperature in an argon-filled glove bag. Sediment subsamples for pore water recovery were taken at a resolution gradually increasing from 1 cm at the surface to 4 cm at the lower end of the core. Additional wet sediment samples were collected in plastic cups of known weight for the determination of water content and porosity by weighing before and after freeze drying. The pore water was extracted by centrifuging and subsequently filtering through 0.2 μm cellulose acetate filters in a second argon-filled glove bag. Total alkalinity was determined onboard by titrating pore water samples with 0.002 M HCl to the equivalent point of carbonic acid. IAPSO standard seawater was used for calibration. Hydrogen sulfide ($\text{TH}_2\text{S} = \text{H}_2\text{S} + \text{HS}^- + \text{S}^{2-}$), ammonium (NH_4^+), ferrous Fe (Fe^{2+}) and silicic acid (H_4SiO_4) were also analyzed onboard by standard photometric techniques⁵⁹. The remaining analyses were realized after the cruise at GEOMAR, if not stated otherwise. Subsamples for sulfate (SO_4^{2-}) and chloride (Cl^-) were kept frozen until analysis by ion chromatography (ECO IC, Metrohm). Subsamples for cation analyses were acidified to pH <2 with distilled concentrated nitric acid and later analyzed by inductively coupled plasma optical emission spectroscopy (ICP-OES, VARIAN 720-ES). The accuracy and precision of anion and cation analyses were evaluated by measuring IAPSO standard seawater.

Carbon concentrations in freeze-dried and ground solid phase samples were analyzed using a EURO EA 3000 Elemental Analyzer. Inorganic carbon was determined by subtracting organic carbon, analyzed after removal of carbonate minerals using 0.5 M hydrochloric acid, from total carbon. For the analysis of total element concentrations in the solid phase by ICP-OES, 100 mg of freeze-dried and ground sample were digested in a closed Teflon vessel containing hydrofluoric acid (40%, supra pure), nitric acid (65%, supra pure) and perchloric acid (60%, p.a.) on a hotplate. The accuracy of the digestion procedure was monitored by inclusion of method blanks and certified reference standards from the Canadian Research Council (PACS-3, MESS-3) as well as the in-house standard OMZ-2. Average values of replicate digestions were generally within the recommended ranges. Major element concentrations in the sediment were corrected for the amount of salt and pore water cations transferred to the solid phase during freeze-drying. To minimize excessive correction factors, fluffy mud samples with very high water content were excluded from Figs. 2 and 4. The mineral content of freeze-dried and ground solid phase samples was evaluated by X-ray diffraction (see Supplementary Methods 1 for further details) at the University of Bremen. Prior to analysis, sediment samples were treated with deionized water at pH 7 in order to remove sea salt transferred from the pore water to the solid phase during freeze drying.

Geochemical modeling

The saturation state of aluminosilicate and carbonate minerals in bottom waters and pore waters of Kiel Bight was evaluated using the geochemical model PHREEQC (Parkhurst and Appelo, 2013). We applied the SIT database implemented in PHREEQC because it includes equilibrium expressions for a large number of relevant minerals and is suitable for the calculation of saturation indices in solution with intermediate ionic strength, such as seawater. Input parameters include measured concentrations of Na^+ , Mg^{2+} , K^+ , Ca^{2+} , Mn^{2+} , Fe^{2+} , Al^{3+} , H_4SiO_4 , SO_4^{2-} , TH_2S and Cl^- as well as alkalinity, pH, temperature and pressure. No pH data were

collected during the research cruise. Therefore, an average pH of 7.5 was adopted, based on prior studies reporting similar values in oxygen-deficient bottom waters⁶⁰ and anoxic pore waters of Kiel Bight⁶¹. A lower pH (~7) may prevail in non-sulfidic surface sediments, whereas a slightly higher pH is observed in strongly sulfidic subsurface sediments (pH >7.7 below 20 cm)⁶². However, varying the adopted pH within this observed range does not affect the interpretation. Due to low dissolved Al concentrations and the limited volume of available pore water, direct analysis of dissolved Al was not possible. Therefore, Al^{3+} was selected to ensure equilibrium with K-rich illite at the depth where both K^+ and H_4SiO_4 concentrations stabilize.

Quantification of cation and alkalinity fluxes

The net rates of K^+ release due to illite dissolution and Mg^{2+} fixation due to montmorillonite precipitation in the sediment were quantified by fitting the general diagenetic equation to our measured pore water profiles. At steady state, the reaction rate R (i.e., K^+ release and Mg^{2+} consumption) is balanced by diffusive and advective transport in the pore water⁶³:

$$\phi R = \phi v \frac{\partial C}{\partial z} - \frac{\partial}{\partial z} \left(\phi D_s \frac{\partial C}{\partial z} \right) \quad (6)$$

In this equation, ϕ is porosity, v is the pore water advection velocity (equals burial velocity after compaction, $\sim 0.2 \text{ cm yr}^{-1}$)³⁶, C is the cation concentration (in $\mu\text{mol cm}^{-3}$), D_s is the diffusion coefficient (in $\text{cm}^2 \text{ yr}^{-1}$) of K^+ or Mg^{2+} in sediments (i.e., corrected for tortuosity⁶⁴ and in-situ temperature, pressure and salinity) and z is sediment depth (in cm). To derive average rates for the entire study area, an exponential function was fit to the asymptotic profiles of porosity and cation concentrations (see Supplementary Methods 2 and Fig. S5). These average profiles of porosity and cation concentrations were then used to solve the diagenetic equation for R. Depth-integrated rates of K^+ release and Mg^{2+} consumption have units of $\mu\text{mol cm}^{-2} \text{ yr}^{-1}$ and equal the upward flux of K^+ and downward flux of Mg^{2+} across the sediment-water interface. Given the hypoxic conditions of bottom waters during the sampling campaign, bioirrigation was excluded from the modeling of cation turnover and benthic fluxes.

Geospatial analyses

To characterize the dominant lithologies along the world's coastlines, we used a medium-resolution global shoreline dataset⁶⁵, which we shifted 1 km inland to maximize spatial overlap with the Global Lithological Map (GLiM)⁵⁶. We then calculated the relative proportions of 13 lithology classes defined in GLiM for both the modern global shoreline and for coastline segments that were covered by ice sheets during the LGM (Table S3). To account for changes in shoreline length due to the inland shift, each shoreline segment was multiplied by the ratio of the original to the shifted shoreline length. The lithology class "carbonate-bearing sedimentary rocks," as referenced in the main text, includes both pure limestone and mixed sediments or sedimentary rocks, such as those eroded in Kiel Bight. An example of coastal lithology in the Baltic Sea region is provided in Fig. S6.

Data availability

All data presented in this article are available in the online database. Pangaea: <https://doi.org/10.1594/PANGAEA.986503>, <https://doi.org/10.1594/PANGAEA.986504>, <https://doi.org/10.1594/PANGAEA.986505>.

Received: 27 June 2025; Accepted: 7 November 2025;

Published online: 26 November 2025

References

1. Fritz, M., Vonk, J. E. & Lantuit, H. Collapsing arctic coastlines. *Nat. Clim. Change* **7**, 6–7 (2017).
2. Nielsen, D. M. et al. Increase in Arctic coastal erosion and its sensitivity to warming in the twenty-first century. *Nat. Clim. Change* **12**, 263–270 (2022).

3. Luetzenburg, G. et al. Sedimentary Coastal Cliff Erosion in Greenland. *J. Geophys. Res. Earth Surf.* **128**, e2022JF007026 (2023).
4. Creel, R. et al. Permafrost thaw subsidence, sea-level rise, and erosion are transforming Alaska's Arctic coastal zone. *Proc. Natl. Acad. Sci.* **121**, e2409411121 (2024).
5. Reyes, F. R. & Loughheed, V. L. Rapid nutrient release from permafrost thaw in arctic aquatic ecosystems. *Arct. Antarct. Alp. Res.* **47**, 35–48 (2015).
6. Laufer-Meiser, K. et al. Potentially bioavailable iron produced through benthic cycling in glaciated Arctic fjords of Svalbard. *Nat. Commun.* **12**, 1349 (2021).
7. Wild, B. et al. Rivers across the Siberian Arctic unearth the patterns of carbon release from thawing permafrost. *Proc. Natl. Acad. Sci.* **116**, 10280–10285 (2019).
8. Tank, S. E. et al. Recent trends in the chemistry of major northern rivers signal widespread Arctic change. *Nat. Geosci.* **16**, 789–796 (2023).
9. Bristol, E. M. et al. Eroding permafrost coastlines release biodegradable dissolved organic carbon to the Arctic Ocean. *J. Geophys. Res. Biogeosci.* **129**, e2024JG008233 (2024).
10. Terhaar, J., Lauerwald, R., Regnier, P., Gruber, N. & Bopp, L. Around one third of current Arctic Ocean primary production sustained by rivers and coastal erosion. *Nat. Commun.* **12**, 169 (2021).
11. Juma, G. A. et al. Future Arctic: how will increasing coastal erosion shape nearshore planktonic food webs?. *Limnol. Oceanogr. Lett.* **10**, 5–17 (2025).
12. L. Oziel et al., Climate change and terrigenous inputs decrease the efficiency of the future Arctic Ocean's biological carbon pump. *Nat. Clim. Change* <https://doi.org/10.1038/s41558-024-02233-6> (2025).
13. Prestrud Anderson, S., Drever, J. I. & Humphrey, N. F. Chemical weathering in glacial environments. *Geology* **25**, 399–402 (1997).
14. Brown, G. H. Glacier meltwater hydrochemistry. *Appl. Geochem.* **17**, 855–883 (2002).
15. Jeandel, C. & Oelkers, E. H. The influence of terrigenous particulate material dissolution on ocean chemistry and global element cycles. *Chem. Geol.* **395**, 50–66 (2015).
16. K. Wallmann, S. Geilert, F. Scholz. Chemical alteration of riverine particles in seawater and marine sediments: effects on seawater composition and atmospheric CO₂. *Am. J. Sci.* **323**, 7 (2023).
17. A. V. Subhas, N. Lehmann, R. E. M. Rickaby, natural analogs to ocean alkalinity enhancement. *Guide to Best Practices in Ocean Alkalinity Enhancement Research 2-oae2023*, 8 (2023).
18. A. Oschlies, L. T. Bach, K. Fennel, J.-P. Gattuso, N. Mengis. Perspectives and challenges of marine carbon dioxide removal. *Front. Clim.* **6**, 1506181 (2025).
19. Mackenzie, F. T. & Garrels, R. M. Chemical mass balance between rivers and oceans. *Am. J. Sci.* **264**, 507–525 (1966).
20. Michalopoulos, P. & Aller, R. C. Rapid clay mineral formation in amazon delta sediments - reverse weathering and oceanic elemental cycles. *Science* **270**, 614–617 (1995).
21. Isson, T. T. & Planavsky, N. J. Reverse weathering as a long-term stabilizer of marine pH and planetary climate. *Nature* **560**, 471–475 (2018).
22. Geilert, S. et al. Coastal El Niño triggers rapid marine silicate alteration on the seafloor. *Nat. Commun.* **14**, 1676 (2023).
23. G. Trapp-Müller, R. C. Aller, A. Sluijs, J. J. Middelburg. silicate weathering and diagenetic reaction balances in deltaic muds. *Am. J. Sci.* **325**, 10 (2025).
24. X. Hu, W.-J. Cai An assessment of ocean margin anaerobic processes on oceanic alkalinity budget. *Glob. Biogeochem. Cycles* **25** (2011).
25. Middelburg, J. J., Soetaert, K. & Hagens, M. Ocean alkalinity, buffering and biogeochemical processes. *Rev. Geophys.* **58**, e2019RG000681 (2020).
26. McManus, J. et al. Early diagenesis of biogenic opal: dissolution rates, kinetics, and paleoceanographic implications. *Deep Sea Res. Part II: Top. Stud. Oceanogr.* **42**, 871–903 (1995).
27. Dale, A. W. et al. Recycling and burial of biogenic silica in an open margin oxygen minimum zone. *Glob. Biogeochem. Cycles* **35**, e2020GB006583 (2021).
28. Meybeck, M. Global chemical weathering of surficial rocks estimated from river dissolved loads. *Am. J. Sci.* **287**, 401–428 (1987).
29. Gaillardet, J., Dupré, B., Louvat, P. & Allègre, C. J. Global silicate weathering and CO₂ consumption rates deduced from the chemistry of large rivers. *Chem. Geol.* **159**, 3–30 (1999).
30. Sun, X., Higgins, J. & Turchyn, A. V. Diffusive cation fluxes in deep-sea sediments and insight into the global geochemical cycles of calcium, magnesium, sodium and potassium. *Mar. Geol.* **373**, 64–77 (2016).
31. Avers, T., Hofstede, J. L. A., Hinrichsen, A., Reimers, H.-C. & Winter, C. Cliff retreat contribution to the littoral sediment budget along the Baltic Sea Coastline of Schleswig-Holstein, Germany. *J. Mar. Sci. Eng.* **9**, 870 (2021).
32. Rossius, J.-E., Avers, T., Krämer, K. & Winter, C. Event-driven erosion of a glacial till cliff. *Geomorphology* **473**, 109626 (2025).
33. Livingstone, S. J., Piotrowski, J. A., Bateman, M. D., Ely, J. C. & Clark, C. D. Discriminating between subglacial and proglacial lake sediments: an example from the Dänischer Wohld Peninsula, northern Germany. *Quat. Sci. Rev.* **112**, 86–108 (2015).
34. E. Seibold et al. "Marine geology of Kiel bay" In *Sedimentology of Parts of Central Europe, Guidebook VIII International Sedimentology Congress* (Kramer, 1971).
35. F. Scholz et al. Benthic-pelagic coupling and isotopic fractionation of barium in Kiel Bight, SW Baltic Sea. *Front. Mar. Sci.* **10**, 1101095 (2023).
36. Fleischmann, S., Scholz, F., Du, J., Scholten, J. & Vance, D. Processes controlling nickel and its isotopes in anoxic sediments of a seasonally hypoxic bay. *Geochim. Cosmochim. Acta* **391**, 1–15 (2025).
37. Lennartz, S. T. et al. Long-term trends at the Boknis Eck time series station (Baltic Sea), 1957-2013: does climate change counteract the decline in eutrophication?. *Biogeosciences* **11**, 6323–6339 (2014).
38. Wallmann, K. et al. Silicate weathering in anoxic marine sediments. *Geochim. Cosmochim. Acta* **72**, 2895–2918 (2008).
39. Scholz, F., Hensen, C., Schmidt, M. & Geersen, J. Submarine weathering of silicate minerals and the extent of pore water freshening at active continental margins. *Geochim. Cosmochim. Acta* **100**, 200–216 (2013).
40. Torres, M. E. et al. Silicate weathering in anoxic marine sediment as a requirement for authigenic carbonate burial. *Earth Sci. Rev.* **200**, 102960 (2020).
41. Michalopoulos, P. & Aller, R. C. Early diagenesis of biogenic silica in the Amazon delta: alteration, authigenic clay formation, and storage. *Geochim. Cosmochim. Acta* **68**, 1061–1085 (2004).
42. Spiegel, T. et al. Updated estimates of sedimentary potassium sequestration and phosphorus release on the Amazon shelf. *Chem. Geol.* **560**, 120017 (2021).
43. Wu, X. et al. Strong potassium uptake in surface sediments of the Changjiang River Estuary and the East China Sea: Implications for authigenic processes and the marine potassium budget. *Earth Planet. Sci. Lett.* **657**, 119292 (2025).
44. D. L. Parkhurst, C. Appelo Description of input and examples for PHREEQC version 3—a computer program for speciation, batch-reaction, one-dimensional transport, and inverse geochemical calculations. In *US Geological Survey techniques and methods*, p 497 (2013).
45. K. Wallmann et al. Erosion of carbonate-bearing sedimentary rocks may close the alkalinity budget of the Baltic Sea and support atmospheric CO₂ uptake in coastal seas. *Front. Mar. Sci.* **9**, 968069 (2022).

46. Lunstrum, A. & Berelson, W. CaCO₃ dissolution in carbonate-poor shelf sands increases with ocean acidification and porewater residence time. *Geochim. Cosmochim. Acta* **329**, 168–184 (2022).
47. Dale, A. W. et al. Seafloor alkalinity enhancement as a carbon dioxide removal strategy in the Baltic Sea. *Commun. Earth Environ.* **5**, 452 (2024).
48. Aparicio, M. et al. Contribution of sandy beaches to the global marine silicon cycle. *Nat. Geosci.* **18**, 154–159 (2025).
49. Bayon, G. et al. Sr/Ca and Mg/Ca ratios in Niger Delta sediments: implications for authigenic carbonate genesis in cold seep environments. *Mar. Geol.* **241**, 93–109 (2007).
50. Berg, R. D., Solomon, E. A. & Teng, F.-Z. The role of marine sediment diagenesis in the modern oceanic magnesium cycle. *Nat. Commun.* **10**, 4371 (2019).
51. Fuhr, M. et al. Calcite is an efficient and low-cost material to enhance benthic weathering in shelf sediments of the Baltic Sea. *Commun. Earth Environ.* **6**, 106 (2025).
52. Prémaillon, M., Regard, V., Dewez, T. J. B. & Auda, Y. GlobR2C2 (Global Recession Rates of Coastal Cliffs): a global relational database to investigate coastal rocky cliff erosion rate variations. *Earth Surf. Dynam.* **6**, 651–668 (2018).
53. J. Ehlers, P. L. Gibbard, P. D. Hughes. Quaternary glaciations - extent and chronology: a closer look. **15**, p 1126 (Elsevier, 2011).
54. Harris, P. T., Macmillan-Lawler, M., Rupp, J. & Baker, E. K. Geomorphology of the oceans. *Mar. Geol.* **352**, 4–24 (2014).
55. Börker, J., Hartmann, J., Amann, T. & Romero-Mujalli, G. Terrestrial sediments of the earth: development of a global unconsolidated sediments map database (GUM). *Geochem. Geophys. Geosyst.* **19**, 997–1024 (2018).
56. J. Hartmann, N. Moosdorf. The new global lithological map database GLiM: a representation of rock properties at the earth surface. *Geochemistry, Geophysics, Geosystems* **13** (2012).
57. Müller, J. D., Schneider, B. & Rehder, G. Long-term alkalinity trends in the Baltic Sea and their implications for CO₂-induced acidification. *Limnol. Oceanogr.* **61**, 1984–2002 (2016).
58. Olafsson, J., Olafsdottir, S. R., Takahashi, T., Danielsen, M. & Arnarson, T. S. Enhancement of the North Atlantic CO₂ sink by Arctic waters. *Biogeosciences* **18**, 1689–1701 (2021).
59. K. Grasshoff, M. Erhardt, K. Kremling. Methods of seawater analysis (Wiley-VCH, Weinheim, ed. 3, 1999).
60. Melzner, F. et al. Future ocean acidification will be amplified by hypoxia in coastal habitats. *Mar. Biol.* **160**, 1875–1888 (2013).
61. Preisler, A. et al. Biological and chemical sulfide oxidation in a Beggiatoa inhabited marine sediment. *ISME J.* **1**, 341–353 (2007).
62. Fuhr, M. et al. Disentangling artificial and natural benthic weathering in organic rich Baltic Sea sediments. *Front. Clim.* **5**, 61 (2023).
63. R. A. Berner. Early diagenesis: a theoretical approach (Princeton University Press, 1980).
64. Boudreau, B. P. The diffusive tortuosity of fine-grained un lithified sediments. *Geochim. Cosmochim. Acta* **60**, 3139–3142 (1996).
65. Wessel, P. & Smith, W. H. F. A global, self-consistent, hierarchical, high-resolution shoreline database. *J. Geophys. Res. Solid Earth* **101**, 8741–8743 (1996).
66. F. Tauber. Meeresbodensedimente in der deutschen Ostsee. Maßstab 1:100000. (Bundesamt für Seeschifffahrt und Hydrographie, 2012).
67. J. L. Sarmiento, N. Gruber, *Ocean Biogeochemical Dynamics* (Princeton University Press, 2006), pp. 528.

Acknowledgements

We would like to thank the crew of RV Alkor for supporting our work at sea, as well as our colleagues Anke Bleyer, Jun Cheng, Sarah Fleischmann, Anna-Kathrin Retschko, Regina Surberg and Paul Vosteen for their assistance with sampling and laboratory analyses. The comments of three anonymous reviewers helped us to improve the manuscript. This study was supported by the German Research Foundation through the Emmy Noether Research Group ICONOX (Iron Cycling in Continental Margin Sediments and the Nutrient and Oxygen Balance of the Ocean). We acknowledge financial support from the Open Access Publication Fund of the University of Hamburg.

Author contributions

F.S. conceptualized the study, secured funding, coordinated the sampling campaigns, interpreted the data, and wrote the manuscript. J.B. carried out the geospatial analyses. C.V. conducted the mineralogical analyses. J.H. provided resources. K.W. offered expertise in RTM and contributed to the interpretation of data. All authors contributed to the manuscript through editing and critical review.

Funding

Open Access funding enabled and organized by Projekt DEAL.

Competing interests

The authors declare no competing interests.

Additional information

Supplementary information The online version contains supplementary material available at <https://doi.org/10.1038/s43247-025-03009-2>.

Correspondence and requests for materials should be addressed to Florian Scholz.

Peer review information *Communications Earth and Environment* thanks the anonymous reviewers for their contribution to the peer review of this work. Primary Handling Editors: Sophia Johannessen and Alice Drinkwater. [A peer review file is available].

Reprints and permissions information is available at <http://www.nature.com/reprints>

Publisher's note Springer Nature remains neutral with regard to jurisdictional claims in published maps and institutional affiliations.

Open Access This article is licensed under a Creative Commons Attribution 4.0 International License, which permits use, sharing, adaptation, distribution and reproduction in any medium or format, as long as you give appropriate credit to the original author(s) and the source, provide a link to the Creative Commons licence, and indicate if changes were made. The images or other third party material in this article are included in the article's Creative Commons licence, unless indicated otherwise in a credit line to the material. If material is not included in the article's Creative Commons licence and your intended use is not permitted by statutory regulation or exceeds the permitted use, you will need to obtain permission directly from the copyright holder. To view a copy of this licence, visit <http://creativecommons.org/licenses/by/4.0/>.

© The Author(s) 2025